CAAP Annual Report

Date of Report: July 19, 2016

Contract Number: DTPH5614HCAP03

Prepared for: Government Agency: DOT

Project Title: Experimental Characterization and Monitoring of Early Stage Corrosion Degradation of Pipeline Steels

Prepared by: Iowa State University

Contact Information: Professor Ashraf Bastawros,
T.A.Wilson Professor of Engineering and Associate Chair for Resrach,
Department of Aerospace Engineering
2271 Howe Hall, Rm 1200
Ames, IA 50011-2271
Phone: 515-294-3039 Fax: 515-294-3262
Email: bastaw@iastate.edu

For quarterly period ending: June 30, 2016

Business and Activity Section

(a) Generated Commitments - None to report

(b) Status Update of Past Quarter Activities - The main objective of the proposed work is to enhance the pipeline safety through understanding the early corrosion mechanisms in high strength pipeline steels that lead to stress corrosion cracking with a focus on measurable degradation parameters that can guide the development of advanced NDE measurement procedures.

The focus of this quarter was to reconcile the differences between the observed compressive residual stresses observed during the early stage of the SCC and the continued progression of subsurface damage and SCC evolution. Our main effort will focus on characterizing the near-surface damage evolution, and the associated mechanical property change within the grains and in the vicinity of the grain boundaries. This will be done by shallow sectioning of the corroded surface, then perform detailed scanning electron microscopy (SEM) and energy-dispersive X-ray spectroscopy (EDS).

Within the experimental observation window, we have identified the following major aspect for the early stage of SCC:

1. The detailed morphological and microstructure examination showed that the entire process is accelerating the grain boundary grooving with evolution of chemical product wedges around grain boundaries.
2. The electrochemical corrosion-process is accompanied by an overall compressive residual stresses, which continue to amplify as the process progress. Such compressive residual stress is favorable to hinder the growth of further cracking. However, the nano- mechanical measurements probes showed that the volumetric expansion of the oxide resulted in tensile opening of the grain boundaries, while exposing the bulk of the surface grains to compressive stresses. Such wedging effect is one of the most significant mechanisms, driving the progression of SCC.
3. Within the laboratory observation time scale and conditions, the grain grooving extended to few microns in depth.
4. The electrochemical corrosion process has resulted in a soft layer near the surface with lower hardness (or flow stress). The nano-probe measurements showed about 20% drop in hardness, with no measureable changes in the elastic modulus. Our speculation is that the corrosion process has generated excessive atomic vacancies that is responsible for such drop.

b.1 Shallow Angle Polishing of the samples:

We have previously showed that the near-surface of the corroded samples are softened, especially within the region near the grain boundaries (GBs) due to intergranular corrosion activity. From our previous nanoindentation experiments, Fig. 1(a) schematically shows the near-surface damage evolution after a corrosion experiment. The sample surface is covered by the corrosion products and the near surface region underneath the corrosion product layer is expected to be chemically deteriorated. To characterize the extent of such deterioration zone into the base material, one of the 2h corroded samples was polished at a shallow angle, as shown in Fig. 1(a). Figure 1(b) shows SEM image of the polished surface, wherein three different regions can be identified: (i) the deposited layer of corrosion products on top of the sample, (ii) the near surface region of the sample, and (iii) the base region of the sample. A set of higher magnification SEM images are shown in Figures 1(c-g) for the corresponding domains. The top layer of the corrosion products (c, d) exhibits unique roughness and a web cracking due to the drying process of these products. Though their morphologies do not correspond to the underlying structure. The evolution of the corrosion process can be identified on images (e-g). The interface between the corrosion product layer and the near surface region can be identified in Fig. 1(e), where the lightly colored circular features are the grains, with an average size of ~5 μm, surrounded by a darker corrosion product fragments. Figure 1(f) indicates that the corrosion process consumes the GBs and generate soft product layer that were removed by the cleaning process. Figure 1(g), represent the extent of the corrosion process and is close to the base region. On this image, one can clearly identify the deepest point of the GB grooving (a triple junction between grains). Such observations are very clear evidences of the corrosion activity taking place through the GBs as a result of intergranular corrosion activity.

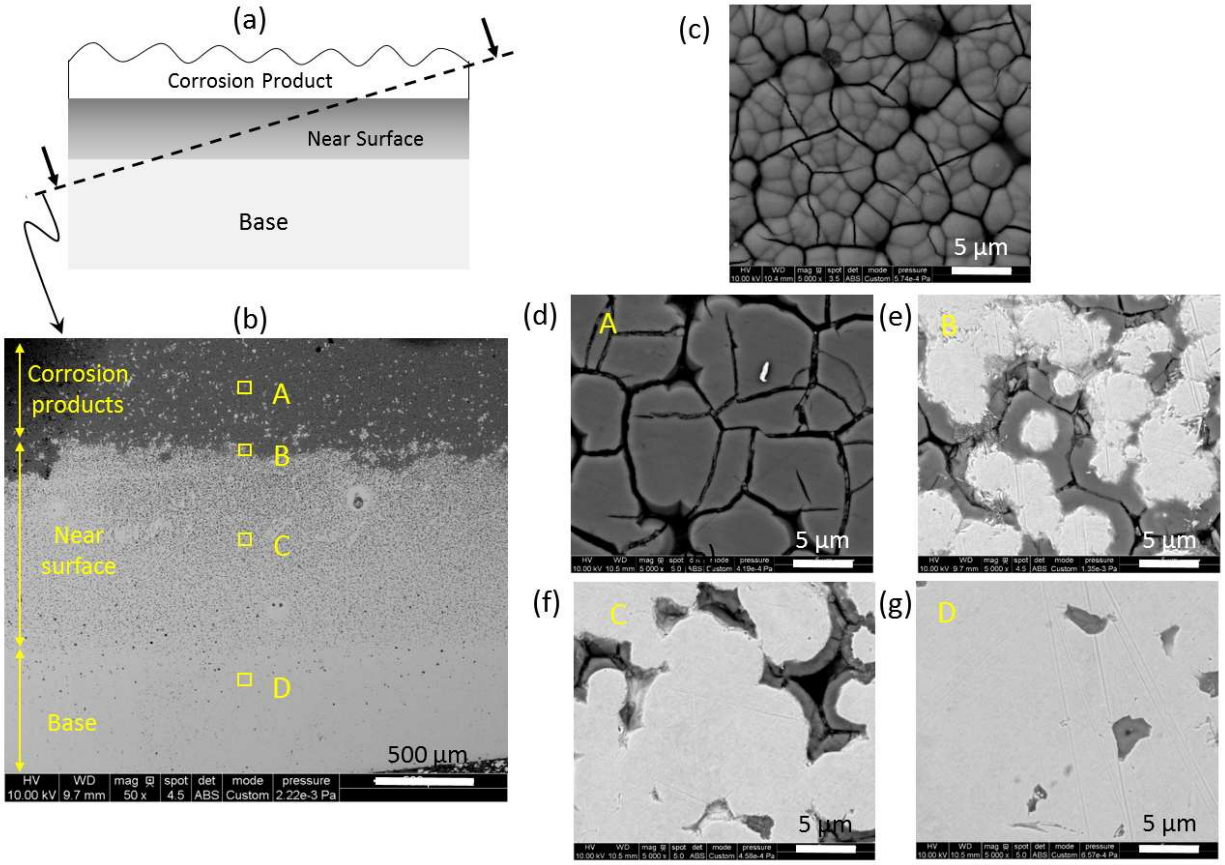

Figure 1: (a) A sketch of the observed near-surface damage evolution as a result of a typical corrosion experiments, and the shallow angle polishing plane. (b) SEM image of the inclined polishing plane, showing locations of high resolution (c-g) SEM images for the progression of the corrosion process into the surface.

b.2 Chemical Composition Analysis by Energy-Dispersive X-ray Spectroscopy:

We have also performed energy-dispersive X-ray spectroscopy (EDS) measurements in order to characterize the chemical composition of the different regions in the near-surface of the samples. Figure 2 shows EDS analysis performed on the top surface of the 2h corroded sample, where both the corrosion product fragments, as well as the base material can be identified. Figure 2(b) show the EDS spectrum of the entire region shown in Fig. 2(a). As can be clearly seen from Figs. 2(b, c), the dominant elements are identified as Oxygen (O), Iron (Fe), and Carbon (C) for the entire area covered by the corrosion products. We previously argued that the corrosion products consist of iron hydroxide ($Fe(OH)_2$), and iron carbonates ($FeCO_3$) according to the reaction scheme proposed by Davies and Burstien [1]. Accordingly, the EDS analyses are very consistent with our previous argument.

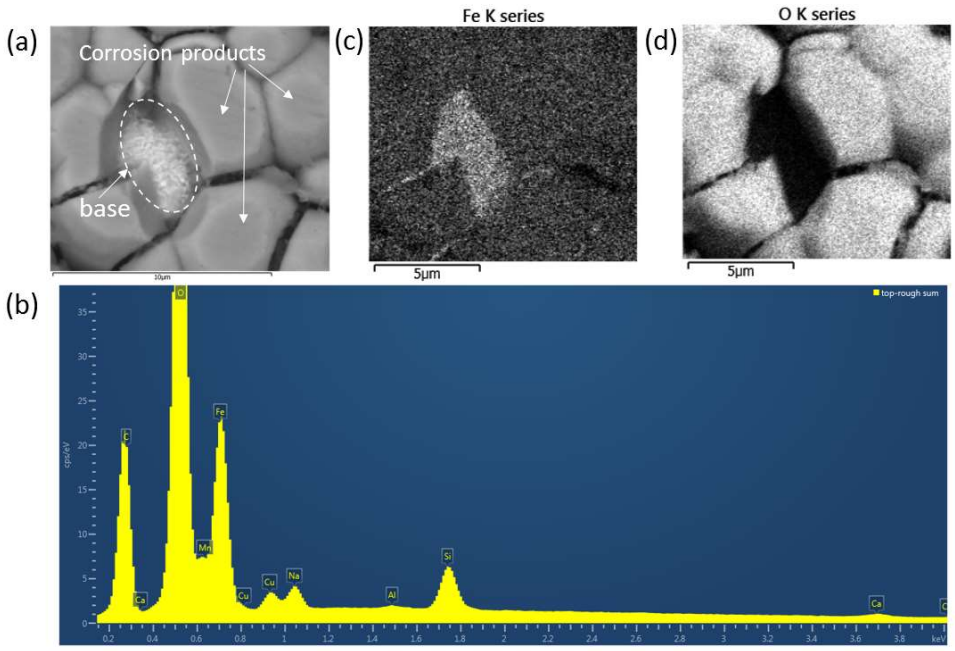

Figure 2: (a) SEM image of the top surface within the corrosion product, and the base material underneath, (b) Energy-dispersive X-ray spectroscopy (EDS) spectrum showing the dominant elements, and EDS maps for (c) Iron (Fe), (d) Oxygen (O).

Another EDS measurement has been performed on the surface of the interface between the corrosion product fragments and the base material grains as shown in Fig. 3(a). As consistent with our SEM observations, the EDS spectrums for the base material grains (G) and the corrosion products (CP) (Fig. 3(b)) and the EDS maps of Fe and O clearly show that there are two distinct regions in terms of chemical composition: (i) the corrosion product fragments (O-enriched), and (ii) the base material grains (trace level of O). Such measurements also demonstrate that the corrosion process happens through the GBs, which is another evidence of intergranular corrosion activity. Finally, we present another EDS measurement performed on the near-surface region as shown in Fig. 4 (a), where the GBs are depleted by the intergranular corrosion activity. The EDS maps of Fe and O clearly show that the corrosion reaction starts at the GBs, which are enhanced by O content, and gradually goes toward the center of the grains.

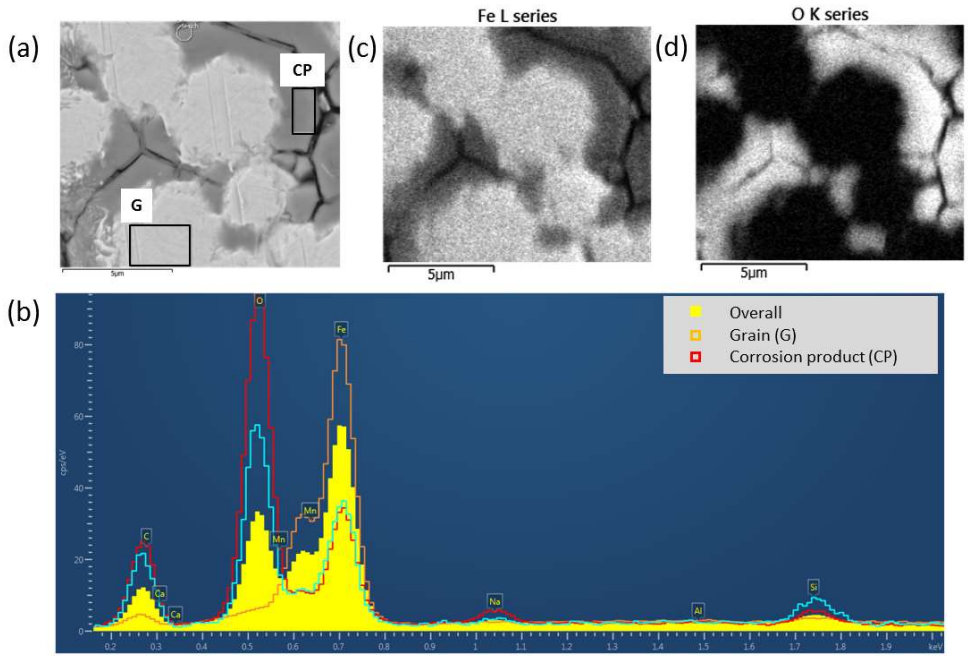

Figure 3: (a) SEM image of the region on the interface between corrosion product particles and the grains (marked as B in Fig. 1(b)). (b) EDS spectrum showing the dominant elements for different region on the (a), (c) EDS map for Iron (Fe), and (d) EDS map for Oxygen (O).

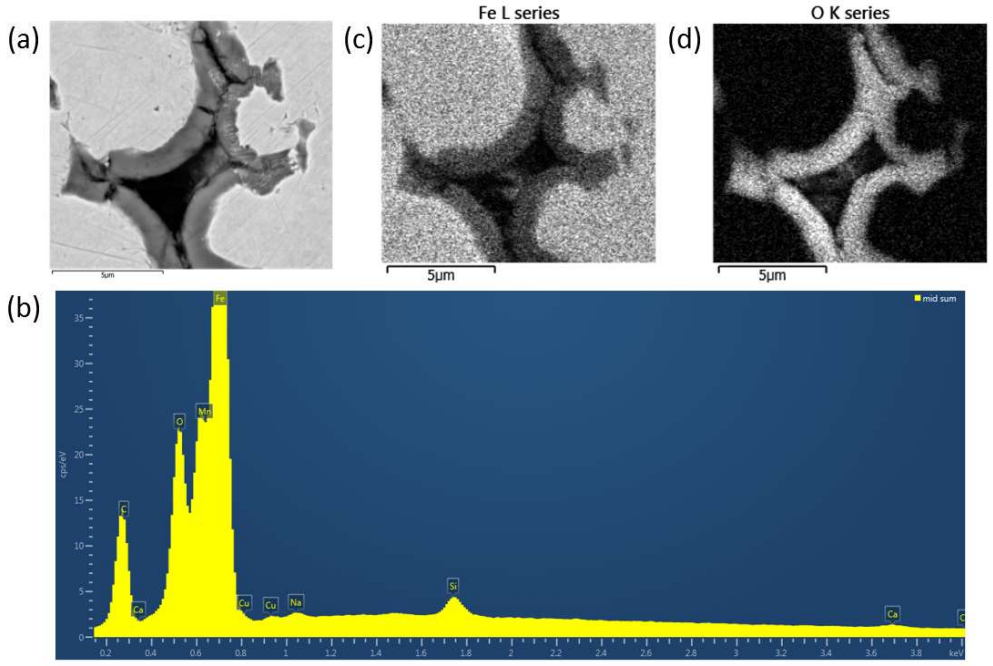

Figure 4: (a) SEM image of the region on the near surface region (marked as C in Fig. 1(b)). (b) EDS spectrum showing the dominant elements, (c) EDS map for Iron (Fe), and (d) EDS map for Oxygen (O).

b.3 Measurement of Near-surface Mechanical Properties by Nano-indentation:

The mechanical properties of these three distinct regions identified by SEM and EDS measurements were firstly characterized by high resolution dynamic nano-indentation technique employing Hysitron nanoDMA® III transducer with 90° cube corner indenter tip. All the indents were placed within the middle of either the fragments (in the corrosion products region) or the grains (in the near surface and base regions). Figures 5 show the variation of the continuously measured modulus, *E*, and hardness, *H*, (derived from the contact analysis by Oliver and Pharr [2]) as a function of indent depth. The black curves correspond to the base region, the blue and red curves correspond to the upper (within the corrosion product layer) and lower parts (down near the base region of Fig. 1) of the near surface region, and the green curves correspond to the corrosion product region. The measured modulus exhibits almost the same level (E~190±10GPa) for both the base and the near surface regions. Such observation shows that the corrosion activity does not have a major effect on the elastic behavior of the material. Moreover, the corrosion product layer has a modulus of about 15% the base material (E~25GPa). It should be noted that the measurements were carried out in the dry state. Therefore, it remains to be seen if the hydroxylated state might exhibit the same stiffness, as such layer may contribute to the balance of the residual stresses developed during the corrosion process.

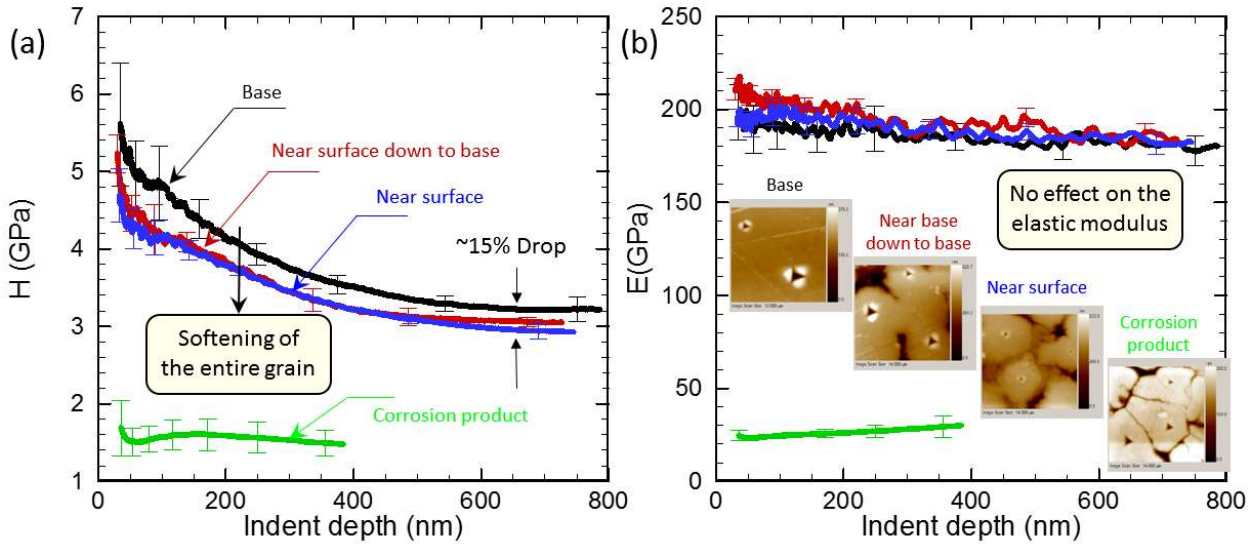

Figure 5: The indentation (a) *H* and (b) *E* as a function of indent depth measured at the different region of the angle polished cross-section: the base region (no corrosion, black), the near-surface region (blue and red), and the corrosion product region (green), the inserts show the indent imprints on the corresponding surfaces.

On the other hand, the measured hardness exhibits many unique features. First, the continuous decay of *H* for the base and near surface regions until reaching a steady state level is a direct manifestation of the size dependent response in this range of measurements [3, 4]. Second, the measured *H* is consistently lower for the near surface region. For the shallow indent depths, the discrepancy between the measured hardness of the base and the near surface regions is around

20%, then becomes 15% as the steady state level is reached. Such observation shows that the entire grain is softened by the intergranular corrosion activity. In addition, the corrosion product layer has a hardness of about 50% the base material (H~1.6GPa) at the steady state level.

b.4 Grain Boundary Damage Evolution

The observation of the enhanced corrosion activity at the GBs may suggest the possibility of the material softening near the GBs. To elucidate such phenomenon, a set of quasi-static shallow indentations was performed on the upper (up to the corrosion product region) and lower parts (down to the base region) of the near-surface region (marked as C in Fig. 1(c)). Nanoindentations were placed on a line traversing the GBs as shown in Figs. 6(c, d), which are atomic force microscope (AFM) images in surface gradient mode rendering of the GBs and the imposed imprints of the indents. The indents were conducted under a constant load of 250 µN and 500 nm apart. This range of loading would limit the indentation to the initial sink-in range [5, 6] as well as limiting the indentation process zone to about 150nm. The variations of E and H for each line across the GB are shown in Figs. 6(a, b), respectively. We have observed two distinct behaviors

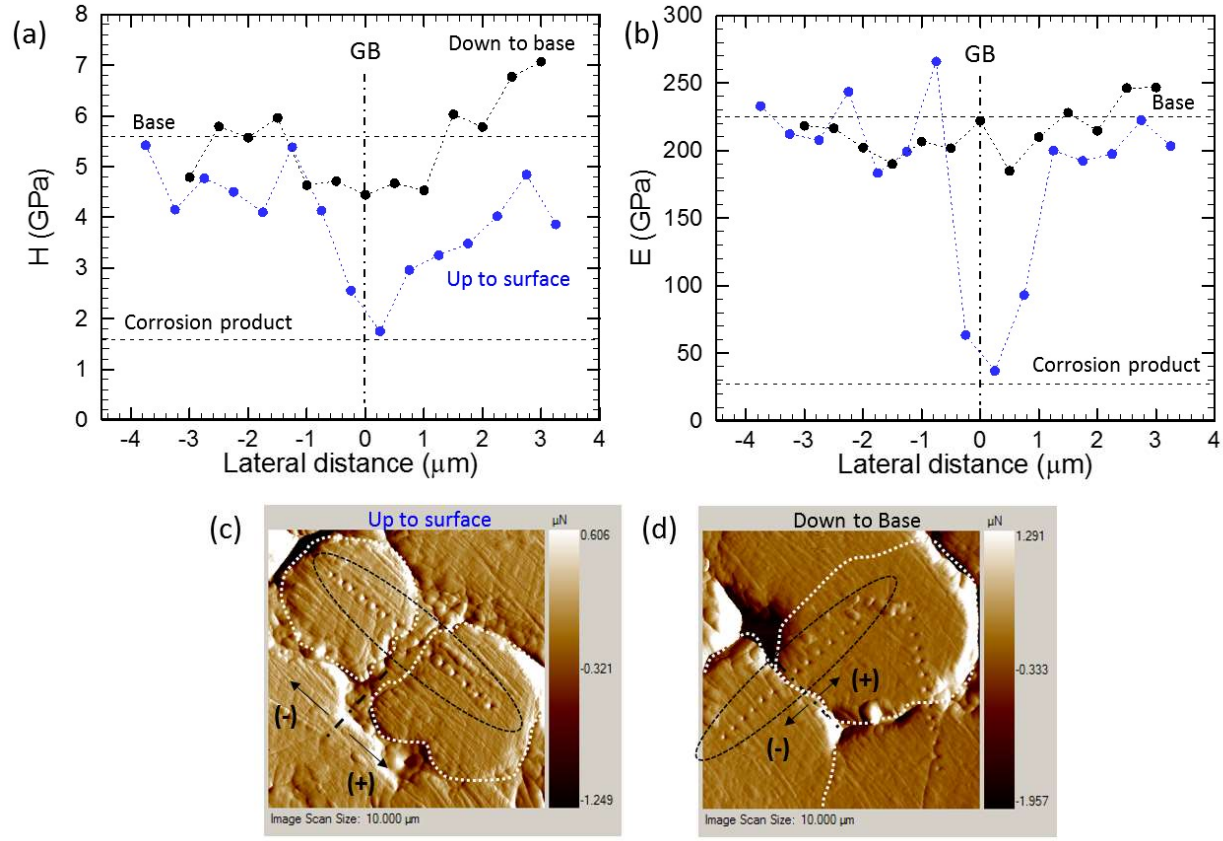

Figure 6: (a, b) The variation of *H* and *E* across the GB measured on the upper (blue, up to the corrosion product region), and lower (black, down to the base region) parts of the near-surface region (marked as C in Fig. 1(b)) and showing the relative reduction compared to the bulk of the grain. (c, d) the corresponding AFM surface gradient showing the line of indent imprints on the region near to the top surface and down to the base on the near surface region (marked as C in Fig. 1(b)), showing the line of indent imprints.

in both measured *E* and *H* depending on the position of the indentations within the near-surface region. The blue points in Figs. 6(a, b) stand for measurements performed on the upper part of the near-surface region. As can be clearly seen, there is a noticeable drop in both quantities across the GB from those in the middle of the grains. The measured *E* and *H* within the grain boundary is very close to those of the corrosion products layer (*E*~25GPa, *H*~1.6GPa). Such drop can be associated with the corrosion products deposited between the GB walls. On the other hand, we have observed a drop only in the measured *H* across the GB for the measurements performed on the lower part of the near-surface region (black points in Figs. 6(a, b)), though this is not as severe as the former one. However, the measured *E* does not show any specific trends as traversing the GB.

We summarize the average levels of the measured *H* and *E* in Fig. 7 for the corrosion products region, upper and lower part of the near-surface region, and the base region. In the near surface region, we report the averaged quantities within the grains and in the vicinity of the GBs separately. In the middle of the grains, similar to our dynamic nano-indentation measurements presented in the previous section, the measured *H* of the near-surface region exhibits a decrease by ~15-20% compared to the base level. In addition, the measured *H* shows a secondary drop in the vicinity of the GBs from that measured in the middle of the grains. On the other hand, the measured *E* of the near surface region is still within the same range with the base level.

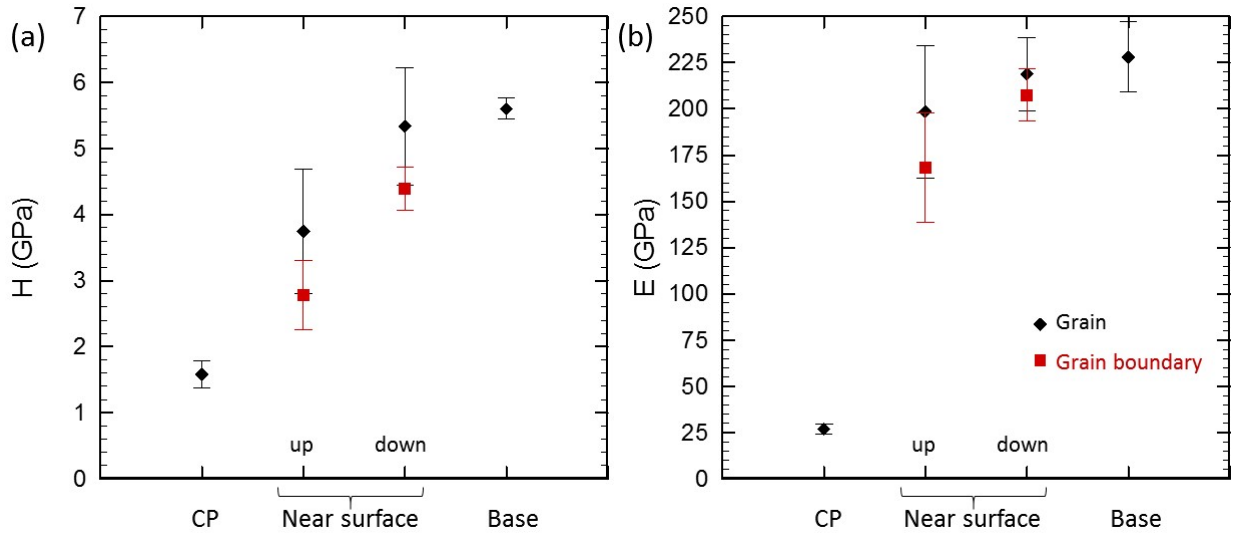

Figure 7: The statistical summary of the measured (a) *H* and (b) *E* on the corrosion product, near-surface (up and down parts are separately presented), and base regions. All measurements are the average with one standard deviation indicated.

Based on all the SEM, EDS, and nanoindentation measurements, Figure 8(a) schematically shows the observed near-surface evolution, where we see the GB grooving due the intergranular corrosion activity and formation of corrosion products between the GB walls. Accordingly, we performed another set of quasi-static shallow indentations on one of these GB grooves close to the

base region (similar to the one shown in Fig. 1(g)). Figure 8(b) is the AFM image in surface gradient mode rendering of the GB. The figure also shows four spatial positions along the GB grooves for a series of nano-indentaion along lines traversing the GB. The indents were similarly conducted under a constant load of 250 µN and 500 nm apart. The variations of *H* and *E* for each line across the GB are shown in Figs. 8(c, d), respectively. There are two types of drops in both quantities across the GB from those in the middle of the grain. The first drop observed throughout the lines 1 and 2 is due to the corrosion products deposited between the GB walls. The measured *H* and *E* are around 1.7 GPa, and 40GPa, respectively, within 1 µm range of the GB. On the other hand, the grain boundary softening is captured by the drop observed throughout the lines 3 and 4. The measured *H* is reduced by 30% within the region near GB region, with an average thickness of 2 µm, then recovered back to the base value in the middle of the grain. However, the measured *E* does not exhibit a noticeable drop in the vicinity of the GB, rather it is ranging within 10% of the base value thought the lines 3 and 4.

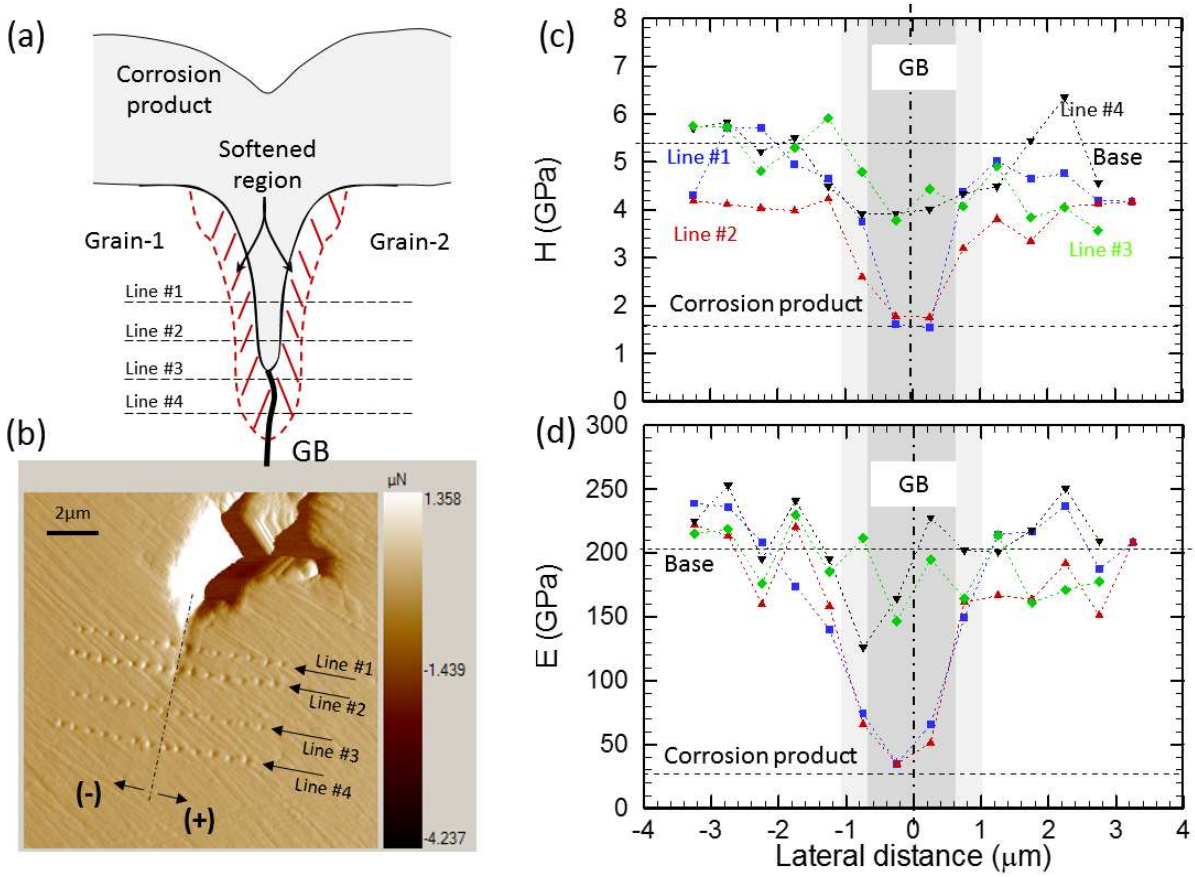

Figure 8: (a) A sketch of the observed near-surface evolution as a result of intergranular corrosion activity, showing the existence of soft layer near the corroded grain boundaries with about 20% drop in hardness, and no measurable changes in modulus. This might be interpreted as excess atomic vacancies near the grain boundaries. (b) the AFM images in surface gradient mode rendering the GB and the imposed lines of indents traversing the GB. The soft layer extends to few microns in depth. (c, d) The variation of *H* and *E* across the GB for each line of indents.

b.5 Summary of Deformation Mechanisms

The electrochemical corrosion process starts aggressively, with cathodic polarization, forming a thin layer of homogeneous corrosion product and momentarily induces tensile residual stress. Then preferential anodic dissolution commences, while being controlled by the differential diffusion of fluxes of both oxygen ions and Fe ions into the GBs. The formation of localized oxides at the GBs with increased volume exerts an overall compressive stresses on the near surface layer. However, at GB interfaces a localized tensile component is generated, leading to continued evolution of the GB grooving process. Such wedging effect is one of the most significant mechanisms, driving the progression of SCC.

(c) Description of any Problems/Challenges – None to report

(d) Planned Activities for the Next Quarter – As we have formulated full chemo-mechanical understanding of the early stage SCC, we will extend the presented cross-sectional analysis to other electrochemical potentials to verify the different aspects of the formulated understanding. The accumulated measurements thus far would be enable the future mathematical formulation and development of analytical predictive tools. A prospective extension of this work would be to a longer time scale and monitor the extent of damage to the range of tens and hundreds of microns. Though that appears to be beyond the current scope of this work.

(e) References Cited

1. Burstein G. T., Davis D. H. The Effects of Bicarbonate on the Corrosion and Passivation of Iron. Corrosion, 36, 416-422 (1980).
2. Oliver W.C., Pharr G.M. An Improved Technique for Determining Hardness and Elastic Modulus using Load and Displacement Sensing Indentation Experiments. Jounal of Material Research, **7**, 1564-1583 (1992).
3. Hall EO (1951) The deformation and ageing of mild steel III. Proc. Phys. Soc. 64: 747-753.
4. Cracknell A, and Petch NJ (1955) Frictional forces on dislocation arrays at the lower yield point in iron, Acta Met. 3:186-189.
5. Yang, C., Lo, C.T., Narasimhan, B., and Bastawros, A.-F., Measurements of Diffusion Thickness at Polymer Interfaces by Nanoindentation: A Numerically Calibrated Experimental Approach, Journal of Materials Research, 24(3), 970-977, (2009).
6. Taljat B., Zacharia T., Pharr G.M., Pile-up behavior of spherical indentations in engineering materials, in Fundamentals of Nanoindentation and Nanotribology, edited by Moody N.R., Gerberich W.W., Burnham N., and Baker S.P. (Mater. Res. Soc. Symp. Proc. 522, Warrendale, PA, 1998), p. 33.